Article

Cumulative polarization in conductive interfacial ferroelectrics

https://doi.org/10.1038/s41586-022-05341-5

Received: 7 April 2022

Accepted: 13 September 2022

Published online: 9 November 2022

Check for updates

Swarup Deb[1,6], Wei Cao[2,6], Noam Raab[1], Kenji Watanabe[3], Takashi Taniguchi[4], Moshe Goldstein[1], Leeor Kronik[5], Michael Urbakh[2], Oded Hod[2] & Moshe Ben Shalom[1]✉

Ferroelectricity in atomically thin bilayer structures has been recently predicted[1] and measured[2–4] in two-dimensional materials with hexagonal non-centrosymmetric unit-cells. The crystal symmetry translates lateral shifts between parallel two-dimensional layers to sign changes in their out-of-plane electric polarization, a mechanism termed 'slide-tronics'[4]. These observations have been restricted to switching between only two polarization states under low charge carrier densities[5–12], limiting the practical application of the revealed phenomena[13]. To overcome these issues, one should explore the nature of polarization in multi-layered van der Waals stacks, how it is governed by intra- and interlayer charge redistribution and to what extent it survives the addition of mobile charge carriers[14]. To explore these questions, we conduct surface potential measurements of parallel WSe_2 and MoS_2 multi-layers with aligned and anti-aligned configurations of the polar interfaces. We find evenly spaced, nearly decoupled potential steps, indicating highly confined interfacial electric fields that provide a means to design multi-state 'ladder-ferroelectrics'. Furthermore, we find that the internal polarization remains notable on electrostatic doping of mobile charge carrier densities as high as 10^{13} cm^{-2}, with substantial in-plane conductivity. Using density functional theory calculations, we trace the extra charge redistribution in real and momentum spaces and identify an eventual doping-induced depolarization mechanism.

Electronic devices based on two-dimensional (2D) materials use electric fields that add/remove mobile charge carriers to control the material conductivity. If these materials also possess switchable electric dipoles, they could serve in future high-density memory technology[13–16]. Therefore, a visionary goal is to design 2D materials that simultaneously show non-volatile memory and rapid logic response where internal charge dipoles and free electrons coexist[17,18]. Such coexistence, however, is typically unfavoured because free charge carriers tend to screen dipole formation and cooperative orientation[19–23]. The recent discovery of interfacial ferroelectricity by interlayer van der Waals sliding suggests an approach to overcome the above difficulty by exploiting a partition between in- and out-of-plane phenomena: in-plane conductivity is afforded by a conducting 2D electron/hole gas, whereas out-of-plane switchable polarization emerges from intrinsic symmetry breaking at the interface that can be controlled by interlayer sliding. This inherent anisotropy of layered ferroelectrics further distinguishes them from thin ferroelectric films, which are highly susceptible to surface/interface depolarization fields[24]. Specifically, at the 2D limit, the polarization magnitude rarely scales with the system thickness and can switch between only two local states[25–27].

Cumulative polarization in trilayers

To explore the potential of interfacial ferroelectrics, we study devices made of two or three transition metal dichalcogenide (TMD) layers that are artificially stacked in a parallel lattice orientation and encapsulated by thin flakes of non-polar hexagonal boron nitride (*h*-BN), placed atop a graphite or gold metallic electrode (Fig. 1a, inset). We measure the room temperature surface potential, roughly 10 nm above the surface, with an atomic force microscope operated in a side-band Kelvin probe mode (Supplementary Information)[2,4]. Fig. 1a presents the obtained potential map, showing a triangular domain landscape of various polarization values, separated by thin domain walls that form owing to a slight twist angle between the flakes. For a sufficiently small global twist, these domain walls accommodate a shear displacement of precisely one interatomic spacing, allowing for perfect AB/BA stacking (zero twist) within the triangular domains[28–30]. The potential profile measured in the top-left triangular region in Fig. 1a (red line) shows two polarization states (Fig. 1b), consistent with previous reports on non-centrosymmetric bilayer TMDs incorporating a single polar interface[1,9,11]. This indicates regions of the WSe_2 trilayer sample where only one of the two interfaces is active, namely showing finite polarization

[1]School of Physics and Astronomy, Tel Aviv University, Tel Aviv, Israel. [2]Department of Physical Chemistry, School of Chemistry, The Raymond and Beverly Sackler Faculty of Exact Sciences and The Sackler Center for Computational Molecular and Materials Science, Tel Aviv University, Tel Aviv, Israel. [3]Research Center for Functional Materials, National Institute for Materials Science, Tsukuba, Japan. [4]International Center for Materials Nanoarchitectonics, National Institute for Materials Science, Tsukuba, Japan. [5]Department of Molecular Chemistry and Materials Science, Weizmann Institute of Science, Rehovoth, Israel. [6]These authors contributed equally: Swarup Deb, Wei Cao. ✉e-mail: moshebs@tauex.tau.ac.il

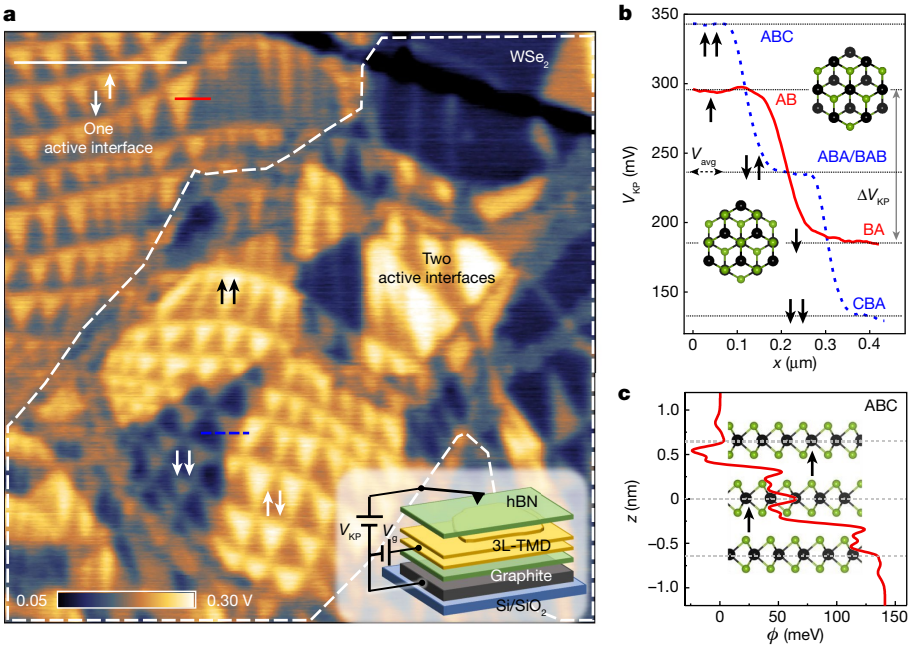

Fig. 1 | Several polarization states in artificially stacked trilayers. a, Surface potential map at the WSe_2 trilayer surface. Dashed white lines mark borders between regions consisting of single and two active interfaces. Arrows denote the out-of-plane polarization orientation in five domains with different stacking configurations. Inset, schematic illustration of the KPFM setup. Scale bar, 0.5 μm. **b**, Typical line cuts of the lateral potential drop across walls separating large domains (extracted from Supplementary Fig. 1f) of single (solid red) and two (dashed blue) active-interface regions. Line cuts crossing domain walls that separate smaller domains are illustrated by the red and dashed blue lines in **a**. The stacking configurations at the corresponding interfaces (shown schematically for the bilayer) are marked beside each potential step, with the corresponding interface polarizations marked by black arrows. **c**, Calculated laterally averaged vertical potential profile along an ABC stacked trilayer with co-oriented (black arrows) interfacial polarization.

due to non-centrosymmetric stacking and in-plane atomic relaxation. Notably, the Kelvin probe profile V_{KP} measured at the central region (dashed blue line) shows three polarization states separated by potential steps of $\Delta V_{KP} \approx 110$ mV (Fig. 1b). The potential of the intermediate step is the average of the two potential values corresponding to a single active-interface trilayer, suggesting two oppositely polarized (↑↓) interfaces within a trilayer WSe_2 region, as for mirror-symmetric Bernal stacking (ABA) of WSe_2. Furthermore, the potential differences between the three polarization states equal those measured at the single active-interface regions, which translates to absolute polarization values twice as large as for the bilayer system. This can be achieved if the two interfaces have parallel polarizations (↑↑, ↓↓), which is the case for the rhombohedral ABC and CBA stacking configurations.

The above experimental evidence indicates that the polarization is localized at the interfaces between layers, indicating a weak coupling between adjacent interfaces and, therefore, a cumulative polarization effect in layered stacks. This is supported by the comparable coverage of the ABC and ABA domains in the map, demonstrating no significant energetic stability preference to either configuration[29,30]. We note, however, that for larger domains, small coverage differences are observed, indicating weak coupling that favours a co-aligned polar ABC configuration over the anti-aligned ABA counterpart (Supplementary Information). Figure 1c presents density functional theory (DFT)-computed potential profiles for the ABC stacked WSe_2 trilayer. The potential drop, $\Delta\phi$, calculated between points far above and below the layered system agrees well with the measured potential drop ($\Delta V_{KP} = 2\Delta\phi$). Its step-like shape[31,32] emphasizes the interfacial confinement of the polarization and hence the weak coupling between adjacent polarized interfaces.

Ladder ferroelectricity in multi-layers

To demonstrate multi-polarization states beyond tri-layered stacks, we measured the potential at the surface of naturally grown ABC stacked (3R-) MoS_2 crystals. The addition of layers with aligned polarization yields an essentially linear increase of the total polarization with stack thickness (Fig. 2a,b,e), confirming the cumulative interfacial effect. Some flake regions show potential values indicative of several interfacial polarization configurations (Fig. 2c,d) of aligned and anti-aligned polarized interfaces. For a given number of layers, regions of different stacking and polarization are spatially separated by local domain walls, whose crossing yields evenly spaced potential steps. The potential value above each region is determined by the difference between upwards ($N_↑$) and downwards ($N_↓$) polarization-pointing active interfaces, which is dictated by the local stacking configuration as extracted from the measured local potential (Fig. 2f). For example, for seven layers ($N = 6$ interfaces), the system can show $N + 1$ polarization values (we note that adding AA' stacked layers does not affect the overall polarization due to mirror symmetry (as in h-BN)). Therefore, by a relative shift of each pair of adjacent layers, one could, in principle[4], increase/decrease the surface potential in a sequential ladder of polarization values.

Polarization and mobile charge doping

The interface-localized nature of the polarization leads to another unusual effect, namely its coexistence with in-plane conductance through the individual layers. We explore this by introducing external gate electrodes to induce free charge carriers in polarized MoS_2 or WSe_2 bilayers. In Fig. 3a–c, we map the surface potential of the same spatial MoS_2 region while applying several fixed gate biases, V_g. Already on application of a relatively small bias, one notices a conductance response (Supplementary Fig. 1c) and an improvement in the map quality (Fig. 3a,b), indicating that the gate bias affects the bilayers carrier density. Application of a larger gate bias leads to domain wall sliding and reversible polarization orientation switching, as reported here and previously for bilayer systems[4–12] (Supplementary Information and Supplementary Fig. 2). ΔV_{KP} measurements under different gate

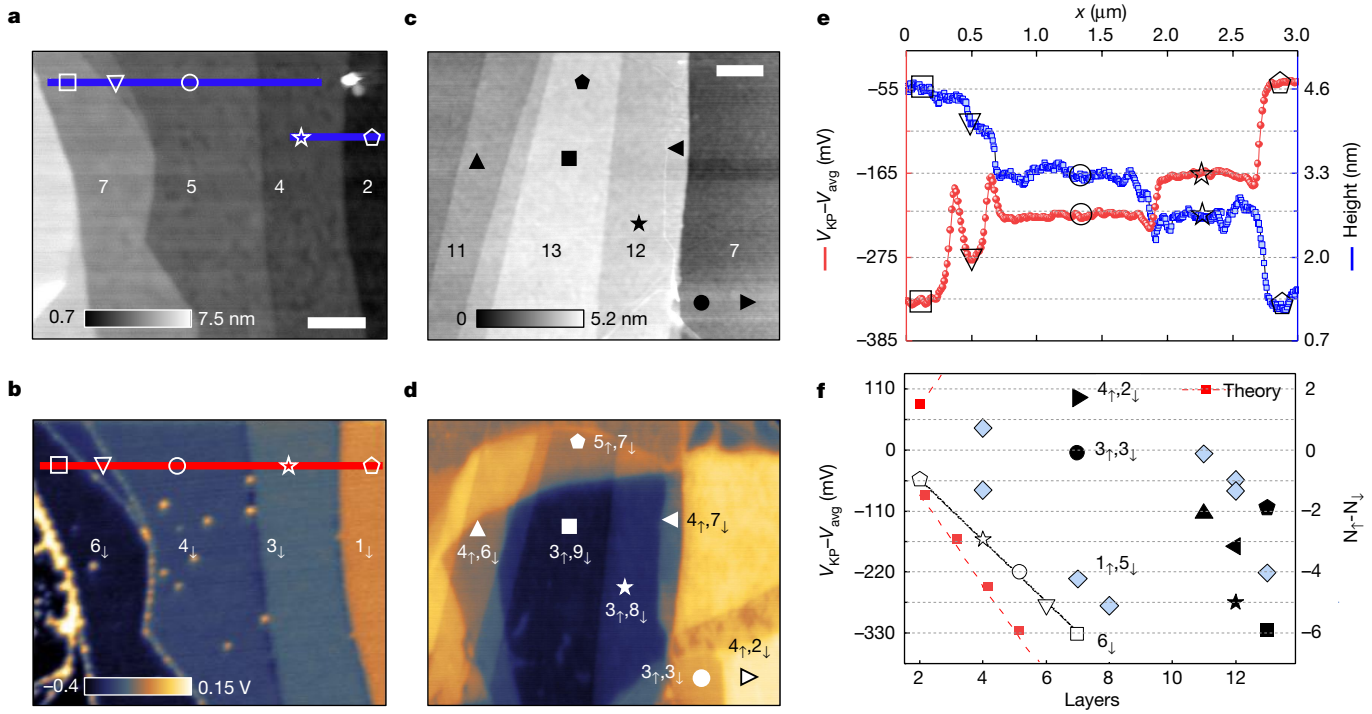

Fig. 2 | Multi-polarization states in naturally grown 3R MoS_2. **a**–**d**, Topography (**a**,**c**) and surface potential (**b**,**d**) maps of two typical flakes composed of 2–7 (**a**,**b**) and 7–13 (**c**,**d**) layers, respectively. Scale bars, **a**,**b**, 0.5 μm; **c**,**d**, 1 μm. The potential is measured relative to the value above an ABA stacked trilayer region (V_{avg} in Fig. 1b). **e**, Line cuts (marked in **a**,**b**) showing the flake thickness (blue squares, right axis) and surface potential (red circles, left axis). The horizontal grids show evenly spaced steps. **f**, Surface potential values and excess number of active interfaces (N↑- N↓) above different positions (as marked in **a**–**d**) versus the number of layers at each point. The dashed black line connects points of the fully co-aligned polar interfaces, where the symbols correspond to those appearing in **a**, **b** and **e**. Other points (with symbols corresponding to **c** and **d**) show fixed, evenly spaced values corresponding to multi-polarization configurations. For example, the four values measured above seven layers with six active interfaces correspond to the $6_\downarrow$, $5_\downarrow1_\uparrow$, $3_\downarrow3_\uparrow$ and $2_\downarrow4_\uparrow$ combinations. Calculated maximal polarization values are indicated by full red squares.

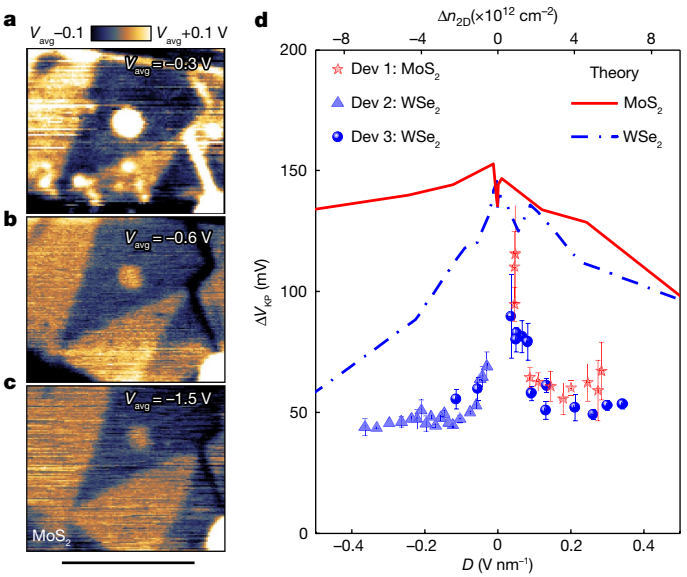

Fig. 3 | Effect of gate bias on the polarization. **a**–**c**, Surface potential maps obtained for bilayer MoS_2 under different gate biases. The centre of the scale bar in each map is set to the corresponding average potential, V_{avg} = −0.3, −0.6, −1.5 V, as indicated in panels **a**,**b**, and **c**, respectively. **a**,**b**,**c** Lower scale bar, 1 μm. **d**, Potential drop, ΔV_{KP}, across domains of opposite polarization (Fig. 1b), as a function of the external displacement field, D, and the corresponding 2D carrier density (lower/upper horizontal axis, Methods). Data from one MoS_2 sample (red stars) and two different WSe_2 samples (blue triangles and circles) are compared to the calculated $2\Delta\phi$ values (solid red, dashed blue lines, respectively).

biases are presented in Fig. 3d for MoS_2 (red stars) and WSe_2 (blue triangles and circles) bilayers. The displacement field, D, and the carrier density, n, for each gate bias are extracted from the average surface potential, V_{avg}, change between the two domains (Fig. 1b). This procedure (Supplementary Information) is insensitive to quantum capacitance or Schottky barrier effects (the latter prevented us from attaining hole doping in MoS_2). Notably, the polarization in both materials is sustained up to the highest experimentally accessible charge density of $n \approx 10^{13}$ cm^{-2}. A reduction of 25–50% in the polarization, however, is observed at $n \approx \pm 3 \times 10^{12}$ cm^{-2}. These findings are in qualitative agreement with DFT calculations, also shown in Fig. 3d, in which doping is introduced by the inclusion of fractional nuclear charge 'pseudoatoms', inducing excess free charge carriers without violating sample neutrality or distorting the underlying band-structure (Supplementary Information)[33]. The experimental polarization provides a lower bound to the true polarization[34], because of limitations of local potential measurements under external bias and screening effects due to surface contaminants accumulating at large carrier densities (Supplementary Information). This explains the underestimation of the experimental measurements with respect to the calculated values. Notably, a qualitative difference between the calculated MoS_2 and WSe_2 polarization response to doping is observed, in which the former shows a weaker response to hole doping than to electron doping, whereas the latter shows an opposite trend.

To rationalize these results, Fig. 4a,b present the calculated laterally averaged excess electron charge density profiles, $\rho_0^{ex}(z)$, for the undoped MoS_2 (Fig. 4a) and WSe_2 (Fig. 4b) bilayers, where $\rho_0^{ex}(z)$ is defined as the difference between the density of the bilayer and the superposition of densities of the corresponding undoped infinitely separated layers (dashed black lines). The excess density features a

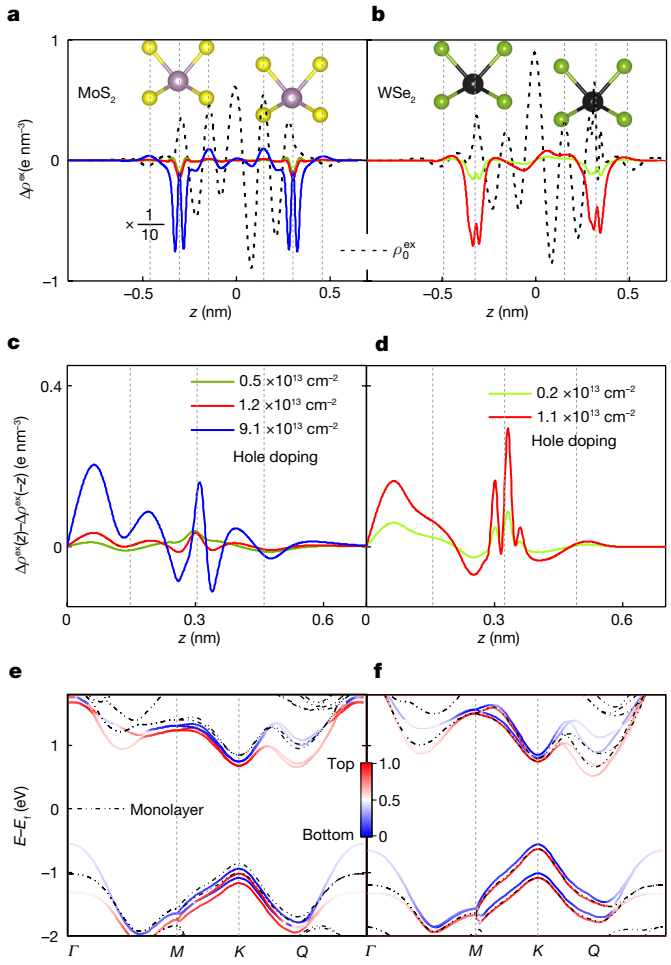

Fig. 4 | Excess charge distribution calculations for polar bilayers of MoS_2 (a,c,e panels) and WSe_2 (b,d,f panels). a,**b**, Laterally averaged excess carrier density profiles of the undoped bilayers, $\rho_0^{ex}(z)$ (dashed black line), defined as the density of the bilayer stack after subtracting the superposition charge density of two isolated layers. Doping-induced variations in the excess carrier density, $\Delta\rho^{ex}(z)$, for different hole densities are represented by the coloured lines (legends in **c** and **d**). All $\Delta\rho^{ex}(z)$ values for MoS_2 are divided by ten for clarity of the representation. **c**,**d**, Doping-induced antisymmetric part of the charge carrier density variation, $\Delta\rho^{ex}(z) - \Delta\rho^{ex}(-z)$, where $z = 0$ is the bilayer centre, for several doping densities. **e**,**f**, Band structures of the undoped bilayer systems, coloured according to the projection of the corresponding crystal momentum state on the top (red) and bottom (blue) layers (text). *K* momentum states split into layer-specific bands (prominent red\blue) that resemble the dashed black bands of a monolayer, only separated by $\approx\frac{e\Delta V_{KP}}{2}$. A larger splitting attributable to strong interlayer-delocalization (designated by nearly white bands) appears for valence *Γ* and conduction *Q* states.

similar prominent asymmetric contribution at the interface between the two layers, for both MoS_2 and WSe_2, which is the origin of the interface dipole shown in Fig. 1c (Supplementary Information). Doping-induced excess charge density variations, $\Delta\rho^{ex}(z)$, are represented by coloured lines for different hole densities. With increasing doping density, excess charge accumulates primarily within the layers at the transition metal plane. To analyse the asymmetry of $\Delta\rho^{ex}(z)$, which is responsible for depolarization, we plot in Fig. 4c,d the antisymmetric part of $\Delta\rho^{ex}(z)$, defined as $\Delta\rho^{ex}(z) - \Delta\rho^{ex}(-z)$, where $z = 0$ is set at the interlayer region centre. For both MoS_2 and WSe_2, the asymmetric part of the excess charge shows two contributions, one at the interface and the other within the layers. We find two important differences in the doping response of $\Delta\rho^{ex}(z)$ in the two materials: (1) at a given hole doping density, the overall charge distribution asymmetry is larger for WSe_2 (compare, for example, the red curves in Fig. 4c,d); and (2) when integrating over the layer region excluding the interface ($z \gtrsim 0.15$ nm) the asymmetric contribution of MoS_2 largely averages out, whereas that of WSe_2 does not. This contribution has a stronger depolarization effect because of its larger distance from the interface. Owing to both factors, depolarization is expected to commence at a significantly lower hole doping value in WSe_2 than MoS_2 (see Supplementary Fig. 8 for comparison).

Finally, to explain the computationally predicted asymmetry between the polarization response to electron and hole doping, we plot in Fig. 4e,f the band structures of the two interfaces, coloured according to the relative contribution of the two layers to each crystal momentum dependent state, $\phi_k(x,y,z)$. To this end, we evaluate its projection on the top layer as $P_k^{Top} = \int_{-\infty}^{\infty} dx \int_{-\infty}^{\infty} dy \int_{0}^{\infty} dz\, |\phi_k(x,y,z)|^2$, with the corresponding projection on the bottom layer given by $P_k^{Bot} = 1 - P_k^{Top}$. This analysis shows that the valence band states at the *Γ* point, Γ_{VB}, which split considerably on the formation of the bilayer structure, are delocalized over both layers. Similar behaviour is found for the conduction band (CB) states at the *Q* point (positioned at the midpoint between the Γ and K points of the Brillouin zone), Q_{CB}, at the bottom of the conduction band[31,32]. Conversely, the corresponding *K*-point states are localized on either of the layers[35] and split to a much smaller extent (comparable to $\Delta V_{KP}/2$), mainly because of the emergent interface dipole (Supplementary Information). Therefore, changes in the occupation of the last states will have a significant effect on the polarization. Fig. 4e shows that for MoS_2 the K_{CB} states are encountered earlier on raising the Fermi level (electron doping), whereas Γ_{VB} states are encountered earlier on lowering the Fermi level (hole doping). This explains the trend observed in Fig. 3d (solid red line), namely that depolarization commences at lower electron doping in MoS_2. Figure 4f predicts an opposite behaviour for WSe_2, owing to a much larger spin-orbit coupling induced upshift of the layer polarized K_{VB} states and downshift of the layer delocalized Q_{CB} states, which explains the trend shown by the dashed blue line in Fig. 3d.

Conclusions

To conclude, we have demonstrated stacked 2D layers that support robust interfacial polarization, which features three unique characteristics: (1) it supports polarization as high as roughly 0.5 pC m^{-1} per interface (Supplementary section 1d,e); (2) it shows distinct and switchable several polarization configurations and (3) it is computationally predicted to sustain charge carrier densities up to 10^{14} cm^{-2}, confirmed by current experimental values as high as 10^{13} cm^{-2}. The coexistence of polarization and conductivity is attributed to the interfacial localization of the polarization and the excess charge carrier delocalization on both layers, which inhibits strong depolarization fields. Notably, the measured polarization and density values are nearly ten times larger than those found for non-hexagonal TMDs to date[5–8,10,12] and may support rich correlated electronic phases[36–38]. Whereas challenges remain, for example, scalability, long-term stability and selective switchability, the cumulative distinct multi-polar ladder of states reported here paves the way to bottom-up construction of three-dimensional multi-ferroic structures out of well-defined 2D building blocks in a controllable, position- and orientation-specific manner.

Online content

Any methods, additional references, Nature Research reporting summaries, source data, extended data, supplementary information, acknowledgements, peer review information; details of author contributions and competing interests; and statements of data and code availability are available at https://doi.org/10.1038/s41586-022-05341-5.

1. Li, L. & Wu, M. Binary compound bilayer and multilayer with vertical polarizations: two-dimensional ferroelectrics, multiferroics, and nanogenerators. *ACS Nano* **11**, 6382–6388 (2017).
2. Woods, C. R. et al. Charge-polarized interfacial superlattices in marginally twisted hexagonal boron nitride. *Nat. Commun.* **12**, 347 (2021).
3. Yasuda, K., Wang, X., Watanabe, K., Taniguchi, T. & Jarillo-Herrero, P. Stacking-engineered ferroelectricity in bilayer boron nitride. *Science* **372**, 1458–1462 (2021).
4. Vizner Stern, M. et al. Interfacial ferroelectricity by van der Waals sliding. *Science* **372**, 142–1466 (2021).
5. Fei, Z. et al. Ferroelectric switching of a two-dimensional metal. *Nature* **560**, 336–339 (2018).
6. Yuan, S. et al. Room-temperature ferroelectricity in $MoTe_2$ down to the atomic monolayer limit. *Nat. Commun.* **10**, 1775 (2019).
7. Sharma, P. et al. A room-temperature ferroelectric semimetal. *Sci. Adv.* **5**, eaax5080 (2019).
8. de la Barrera, S. C. et al. Direct measurement of ferroelectric polarization in a tunable semimetal. *Nat. Commun.* **12**, 5298 (2021).
9. Wang, X. et al. Interfacial ferroelectricity in rhombohedral-stacked bilayer transition metal dichalcogenides. *Nat. Nanotechnol.* **17**, 367–371 (2022).
10. Wan, Y. et al. Room-temperature ferroelectricity in 1T'-ReS_2 multilayers. *Phys. Rev. Lett.* **128**, 067601 (2022).
11. Weston, A. et al. Interfacial ferroelectricity in marginally twisted 2D semiconductors. *Nat. Nanotechnol.* **17**, 390–395 (2022).
12. Lipatov, A. et al. Direct observation of ferroelectricity in two-dimensional MoS_2. *NPJ 2D Mater. Appl.* **6**, 18 (2022).
13. Lines, M. & Glass, A. *Principles and Applications of Ferroelectrics and Related Materials* (Oxford Univ. Press, 2001).
14. Wu, M. & Li, J. Sliding ferroelectricity in 2D van der Waals materials: related physics and future opportunities. *Proc. Natl Acad. Sci. USA* **118**, e2115703118 (2021).
15. Eerenstein, W., Mathur, N. D. & Scott, J. F. Multiferroic and magnetoelectric materials. *Nature* **442**, 759–765 (2006).
16. Setter, N. et al. Ferroelectric thin films: review of materials, properties, and applications. *J. Appl. Phys.* **100**, 051606 (2006).
17. Anderson, P. W. & Blount, E. I. Symmetry considerations on martensitic transformations: 'ferroelectric' metals? *Phys. Rev. Lett.* **14**, 217–219 (1965).
18. Xue, F., He, J. H. & Zhang, X. Emerging van der Waals ferroelectrics: unique properties and novel devices. *Appl. Phys. Rev.* **8**, 021316 (2021).
19. Iwazaki, Y., Suzuki, T., Mizuno, Y. & Tsuneyuki, S. Doping-induced phase transitions in ferroelectric $BaTiO_3$ from first-principles calculations. *Phys. Rev. B. Condens. Matter Mater. Phys.* **86**, 214103 (2012).
20. Wang, Y., Liu, X., Burton, J. D., Jaswal, S. S. & Tsymbal, E. Y. Ferroelectric instability under screened Coulomb interactions. *Phys. Rev. Lett.* (2012).
21. Zhao, H. J. et al. Meta-screening and permanence of polar distortion in metallized ferroelectrics. *Phys. Rev. B.* **97**, 054107 (2018).
22. Shi, Y. et al. A ferroelectric-like structural transition in a metal. *Nat. Mater.* **12**, 1024–1027 (2013).
23. Zhou, W. X. & Ariando, A. Review on ferroelectric/polar metals. *Jpn. J. Appl. Phys.* **59**, SI0802 (2020).
24. Dawber, M., Rabe, K. M. & Scott, J. F. Physics of thin-film ferroelectric oxides. *Rev. Mod. Phys.* **77**, 1083–1130 (2005).
25. Jia, C. L. et al. Unit-cell scale mapping of ferroelectricity and tetragonality in epitaxial ultrathin ferroelectric films. *Nat. Mater.* **6**, 64–69 (2007).
26. Böscke, T. S., Müller, J., Bräuhaus, D., Schröder, U. & Böttger, U. Ferroelectricity in hafnium oxide thin films. *Appl. Phys. Lett.* **99**, 102903 (2011).
27. Liu, F. et al. Room-temperature ferroelectricity in $CuInP_2S_6$ ultrathin flakes. *Nat. Commun.* **7**, 12357 (2016).
28. Alden, J. S. et al. Strain solitons and topological defects in bilayer graphene. *Proc. Natl Acad. Sci. USA* **110**, 11256–11260 (2013).
29. Weston, A. et al. Atomic reconstruction in twisted bilayers of transition metal dichalcogenides. *Nat. Nanotechnol.* **15**, 592–597 (2020).
30. Rosenberger, M. R. et al. Twist angle-dependent atomic reconstruction and moiré patterns in transition metal dichalcogenide heterostructures. *ACS Nano* **14**, 4550–4558 (2020).
31. Ferreira, F., Enaldiev, V. V., Fal'ko, V. I. & Magorrian, S. J. Weak ferroelectric charge transfer in layer-asymmetric bilayers of 2D semiconductors. *Sci. Rep.* **11**, 13422 (2021).
32. Magorrian, S. J. et al. Multifaceted moiré superlattice physics in twisted bilayers. *Phys. Rev. B.* **104**, 125440 (2021).
33. Sinai, O. & Kronik, L. Simulated doping of Si from first principles using pseudoatoms. *Phys. Rev. B - Condens. Matter Mater. Phys.* **87**, 235305 (2013).
34. Collins, L., Kilpatrick, J. I., Kalinin, S. V. & Rodriguez, B. J. Towards nanoscale electrical measurements in liquid by advanced KPFM techniques: a review. *Reports Prog. Phys.* **81**, 086101 (2018).
35. Sung, J. et al. Broken mirror symmetry in excitonic response of reconstructed domains in twisted $MoSe_2$/$MoSe_2$ bilayers. *Nat. Nanotechnol.* **15**, 750–754 (2020).
36. Chen, W. et al. Direct observation of van der Waals stacking–dependent interlayer magnetism. *Science* **366**, 983–987 (2019).
37. Vaño, V. et al. Artificial heavy fermions in a van der Waals heterostructure. *Nature* **599**, 582–586 (2021).
38. Liu, X., Pyatakov, A. P. & Ren, W. Magnetoelectric coupling in multiferroic bilayer VS_2. *Phys. Rev. Lett.* **125**, 247601 (2020).

Methods

Sample preparation

MoS_2 and WSe_2, obtained from HQ Graphene, were exfoliated onto polydimethylsiloxane. Large single-layer flakes (roughly 20 μm or more) of TMDs were identified using optical contrast. *h*-BN flakes were picked up from the substrate using polydimethylsiloxane/poly(methyl methacrylate)-based dry transfer technique and placed on few-layered graphene or predesigned gold electrodes (Supplementary Fig. 1a). Subsequently, parallel bilayers of TMDs were prepared on the *h*-BN surface using the 'tear and stack' technique. The entire stack is then encapsulated with another *h*-BN flake. The bottom graphene or gold substrate acts as a reference electrode for Kelvin probe force microscopy (KPFM) measurements and as a gate electrode. In the trilayer measurements (without doping), the stack was placed directly on the conducting electrode without the bottom *h*-BN.

The samples studied in Fig. 2, with MoS_2 multi-layered systems beyond trilayer stacks, were obtained by exfoliating the 3R single crystal (purchased from HQ Graphene) to a bare SiO_2 surface and connecting the flakes to a metal electrode.

KPFM measurements

KPFM measurements were acquired using a Park System NX10 atomic fluorescence microscope in non-contact scanning mode. The electrostatic signal was measured at side-band frequencies using a built-in lock-in amplifier. We used PointProbe Plus Electrostatic Force Microscopy (PPP-EFM) *n*-doped tips with a conductive coating. The mechanical resonance frequency of the tips was roughly 75 kHz and the force constant was 3 N m^{-1}. The cantilever oscillated mechanically with an amplitude ranging from 20 to 5 nm. In several experiments, the average height above the surface, *h*, was controlled through a two-pass measurement. The first pass records the topography, whereas in the second pass the tip follows the same scan line with a predefined lift (typically 4–5 nm) and measures the KPFM signal. The cantilever was excited with an a.c. voltage to perform KPFM measurements, with an amplitude of 1.5–4 V and a frequency of 2–4 kHz. In the closed-loop measurements, the d.c. voltage was controlled by a bias servo to obtain the surface potential. Images were acquired using the Park SmartScan software and the data were analysed using the Gwyddion program.

Computation

Potential profiles were calculated using the Perdew–Burke–Ernzerhof generalized-gradient exchange-correlation density functional approximation[39], augmented by the Grimme-D3 dispersion correction with Becke–Johnson damping[40] as implemented in the Vienna ab-initio simulation package (VASP)[41]. The core electrons of the Mo, W, S and Se atoms were treated by means of the projector augmented wave approach. Spin-orbit interactions were included. Single-point electron density calculations were performed on relaxed layer structures with a plane wave energy cut-off of 600 eV and a *k*-point mesh of $12 \times 12 \times 1$, setting a vertical vacuum size of 10 nm to avoid interactions between adjacent bilayer images. To evaluate the vertical polarization, a dipole moment correction was used. Doping calculations of bilayer WSe_2 and MoS_2 were performed using the fractional nuclear charge pseudoatom approach[33], allowing for simulating doping densities in the experimentally relevant range. To this end, we use pseudopotentials generated for atoms with fractional nuclear charge, within the open source Quantum Espresso package[42].

Data availability

Source data are provided with this paper.

39. Perdew, J. P., Burke, K. & Ernzerhof, M. Generalized gradient approximation made simple. *Phys. Rev. Lett.* **77**, 3865–3868 (1996).
40. Grimme, S., Antony, J., Ehrlich, S. & Krieg, H. A consistent and accurate ab initio parametrization of density functional dispersion correction (DFT-D) for the 94 elements H-Pu. *J. Chem. Phys.* **132**, 154104 (2010).
41. Kresse, G. & Furthmüller, J. Efficient iterative schemes for ab initio total-energy calculations using a plane-wave basis set. *Phys. Rev. B - Condens. Matter Mater. Phys.* **54**, 11169–11186 (1996).
42. Giannozzi, P. et al. QUANTUM ESPRESSO: a modular and open-source software project for quantumsimulations of materials. *J. Phys. Condens. Matter* **21**, 395502 (2009).

Acknowledgements We thank A. Cerreta (Park Systems) for atomic fluorescence microscopy support and N. Ravid for laboratory support. K.W. and T.T. acknowledge support from JSPS KAKENHI (grant nos. 19H05790, 20H00354 and 21H05233). M.G. has been supported by the Israel Science Foundation and the Directorate for Defense Research and Development grant no. 3427/21 and by the US-Israel Binational Science Foundation grant no. 2020072. L.K. thanks the Aryeh and Mintzi Katzman Professorial Chair and the Helen and Martin Kimmel Award for Innovative Investigation. M.U. acknowledges the financial support of the Israel Science Foundation, grant no. 1141/18, and the binational programme of the National Science Foundation of China and Israel Science Foundation, grant no. 3191/19. O.H. is grateful for the generous financial support of the Israel Science Foundation under grant no. 1586/17, The Ministry of Science and Technology of Israel (project no. 3–16244), the Heineman Chair in Physical Chemistry, and the Naomi Foundation for generous financial support from the the 2017 Kadar Award. M.B.S. acknowledges funding by the European Research Council under the European Union's Horizon 2020 research and innovation programme (grant agreement no. 852925), and the Israel Science Foundation under grant nos. 1652/18 and 3623/21. O.H. and M.B.S. acknowledge the Centre for Nanoscience and Nanotechnology of Tel Aviv University.

Author contributions S.D. and N.R. conducted the experiments supervised by M.B.S. W.C. conducted the DFT calculations supervised by L.K., M.U. and O.H. K.W. and T.T. provided the *h*-BN crystals. S.D., W.C., N.R., M.G., L.K., M.U., O.H. and M.B.S. analysed the data, discussed the results and wrote the manuscript.

Competing interests The authors declare no competing interests.

Additional information
Supplementary information The online version contains supplementary material available at https://doi.org/10.1038/s41586-022-05341-5.

Correspondence and requests for materials should be addressed to Moshe Ben Shalom.

Peer review information *Nature* thanks Erjun Kan and the other, anonymous, reviewer(s) for their contribution to the peer review of this work.